

Auto-Oxygenated Porphyrin-Derived Redox Mediators for High-Performance Lithium Air-Breathing Batteries

Hyun-Soo Kim, Boran Kim, Hyunyoung Park, Jongsoon Kim,* and Won-Hee Ryu*

Because of their distinct energy potentials, Li air-breathing batteries have been highlighted as promising energy storage systems; however, the sluggish oxygen reduction and evolution reactions (ORR and OER) disturb the reversible cell operation during cycling. Therefore, catalyst materials should be tailored to mitigate the low efficiencies of air-breathing batteries. A porphyrin-derived catalyst is optimized by introducing different metal-centered organometallic phthalocyanine (MPc) complexes and their potential application as redox mediators (RMs) for fabricating efficient Li–O₂ cells is investigated. The feasibility of each MPc is determined as a potential RM by calculating its orbital levels. The electrochemical properties of the Li–O₂ cells employing the diverse MPc-RMs are compared. The MPc-containing Li–O₂ cells exhibit improved cell performance, reduced polarization, and stable cyclability with auto-oxygenated properties as revealed by directly injecting superoxide species into the MPc-containing electrolytes. The synergistic effects of blended MPcs—a mixture consisting of the two most effective MPcs—in both the OER and ORR regions in ambient air atmosphere are also elucidated. The reaction mechanism of the MPc-containing cells is proposed based on first-principles calculations and experimental results. The introduction of natural functional catalysts provides a basis for developing effective eco-friendly catalysts for application to sustainable air-breathing batteries.

air-breathing batteries (LABs), also called lithium–oxygen (Li–O₂) batteries (LOBs), have been recognized as one of the most promising high-efficiency ESSs because of (i) application of infinite and easy-accessible oxygen gases as the cathode and (ii) large gravimetric energy densities (>3500 Wh kg^{−1}) and volumetric energy densities (>6900 Wh L^{−1}) by the application of lightweight elements such as Li and O.^[2] Reportedly, the LAB reaction mechanism is based on the following reversible conversion from/to the gas phase to/from the solid phase: $x\text{Li}^+ + \text{O}_2 (\text{gas}) + xe^- \leftrightarrow \text{Li}_x\text{O}_2 (\text{solid})$ (where $x = 1$ or 2).^[3] However, despite the merit of the high gravimetric energy densities, LABs exhibit large overpotentials and a poor cycling life because it is difficult to decompose the solid Li_xO₂ insulating phase during charging.^[4]

To solve these problems, various catalysts have been investigated for the facile and efficient decomposition of Li_xO₂ phases.^[5] Because of their widespread application to oxygen evolution reactions (OERs) in fuel cells and water splitting, solid catalysts have been widely studied

to lower LAB overpotentials.^[6] However, they also reportedly promote the decomposition of not only Li_xO₂ but also the electrolyte solvent.^[7] Furthermore, the limited contact between the solid catalyst and the solid Li_xO₂ phase hinders the theoretical catalytic activity for Li_xO₂ decomposition.^[8] Recently, soluble catalysts or redox mediators (RMs) have attracted considerable attention as promising catalysts for improving LAB electrochemical performance because of the efficient liquid–solid contact achieved by direct dissolution in the liquid electrolyte and the prevention of passivation by discharge products.^[8a,9] Reportedly, RMs can provide electrochemical detours to lower LAB overpotentials through direct reduction or oxidation during discharging or charging, respectively ($\text{RM} + e^- \rightarrow \text{RM}^{\text{red}}$, $\text{RM} \rightarrow \text{RM}^{\text{ox}} + e^-$) instead of decomposing Li_xO₂.^[10] Then, the reduced or oxidized RM intermediates are directly diffused to discharge products to/from which they chemically donate or accept electrons as follows: ($2\text{RM}^{\text{red}} + x\text{Li}^+ + \text{O}_2 \rightarrow 2\text{RM} + \text{Li}_x\text{O}_2$, $2\text{RM}^{\text{ox}} + \text{Li}_x\text{O}_2 \rightarrow 2\text{RM} + x\text{Li}^+ + \text{O}_2$). Most RMs are mainly based on benzene-ring-containing organic compounds owing to their solubility in organic liquids and extra electrons.^[8a,9b,11] However, electron insertion/extraction into/from the benzene ring can affect bonding environments among organic elements, which may destabilize the molecular structure of organic-based RMs

1. Introduction

With the explosive growth in demand for efficient energy storage systems (ESSs) for portable electronic devices and grid-scale applications, many researchers have focused on high-efficiency ESSs beyond Li-ion batteries (LIBs).^[1] Lithium

H.-S. Kim, B. Kim, W.-H. Ryu
Department of Chemical and Biological Engineering
Sookmyung Women's University
100 Cheongpa-ro 47-gil, Yongsan-gu, Seoul 04310, Republic of Korea
E-mail: whryu@sookmyung.ac.kr

H. Park, J. Kim
Department of Energy Science
Sungkyunkwan University
2066 Seobu-ro, Jangan-gu, Suwon 16419, Republic of Korea
E-mail: jongsoonkim@skku.edu

W.-H. Ryu
Institute of Advanced Materials and Systems
Sookmyung Women's University
100 Cheongpa-ro 47-gil, Yongsan-gu, Seoul 04310, Republic of Korea

 The ORCID identification number(s) for the author(s) of this article can be found under <https://doi.org/10.1002/aenm.202103527>.

DOI: 10.1002/aenm.202103527

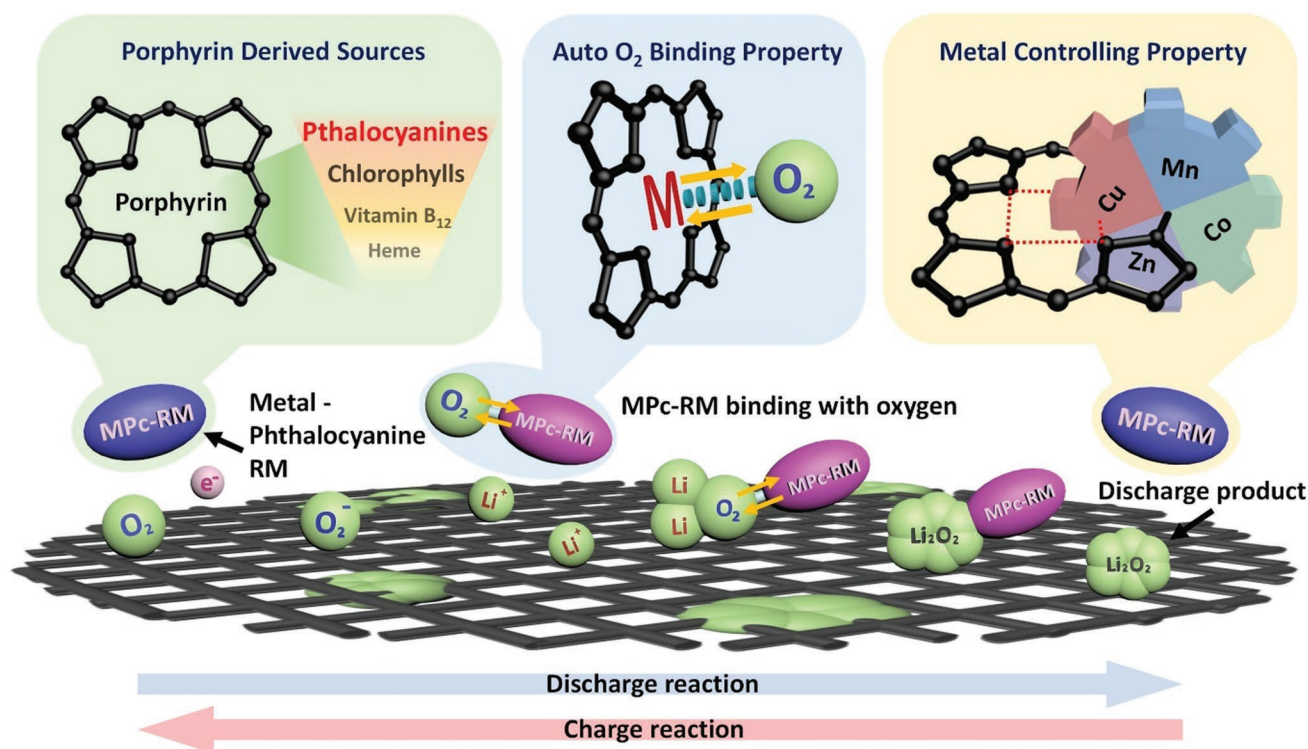


Figure 1. Representative properties of metal phthalocyanine redox mediators (MPc-RMs) and schematic illustrating reaction mechanisms in Li–O₂ cells.

during repeated LAB charging–discharging cycles. This suggests that it is more important to develop RMs that provide electrons more stably during charging–discharging than to simply use organic-based RMs to enhance LAB electrochemical performance.

Therefore, this study aimed to discover organometallic compounds that are promising RMs for application to high-performance LABs. Owing to a central metal atom, the proposed RMs exhibited stable electron extraction/insertion, structural stability, high solubility in organic solvents, and auto-oxygenation—even in low-O₂ environments such as ambient air.^[12] Herein, we used first-principles calculations and conducted various experiments to demonstrate that organometallic phthalocyanine complexes ((C₈H₄N₂)₄M (= MPc), where M = Mn, Co, Cu, and Zn) could be applied as promising RMs. In particular, MnPc and ZnPc contain low-cost metals, implying that their high price competitiveness as promising catalysts than other organometallic-based RMs. Because pristine and oxidized MPc exhibited appropriate highest occupied molecular orbital (HOMO) energy levels, the overpotentials of MnPc and ZnPc applied in LAB were considerably lower than those of the LABs without RMs. Moreover, the cyclability of LABs was remarkably enhanced by optimally combining MnPc and ZnPc in a low-O₂ (<20 vol.%) ambient atmosphere. The cell fabricated using the blended MPcs exhibited effective catalytic activities in both the oxygen evolution reaction (OER) and oxygen reduction reaction (ORR) regions with stable cyclability over 60 cycles. The reaction pathway of the MPc-containing cell was also proposed based on thermodynamics energy diagrams and experimental results. Our study provides new insights into the introduction

of nature-derived phthalocyanine catalysts and contributes to the development of binary soluble catalysts for environmental-friendly and cost-effective air-breathing battery technology.

2. Results and Discussion

2.1. Merits of MPcs as Promising RMs for Application to LABs

As shown in **Figure 1**, the basic MPc molecular structure is based on an aromatic organic compound structurally related to porphyrins.^[13] The existence of transition metal compounds in the center of MPcs can result in auto-O₂-binding properties because transition metals easily oxidize or reduce to stably share electrons with O₂ molecules.^[14] Moreover, it has been suggested that the overall MPc properties could be controlled by controlling the central transition-metal atom in the molecular structure, which implies that well-controlled MPcs can deliver excellent catalytic activities and high stability for application to LABs and exhibit a wide range of redox potentials by manipulating the central metal atom.^[15] Thus, to discover effective and outstanding MPcs as promising RMs for application to LABs, we performed first-principles calculations on various MPcs exhibiting different central transition-metal atoms. **Figure 2a–d** presents various MPc structures including CoPc, CuPc, MnPc, and ZnPc composed of a central metal atom coordinated with four nitrogen atoms. To determine the feasibility of using diverse MPcs as potential soluble catalysts for application to Li–O₂ batteries, we considered the TEGDME-based electrolyte and used the TEGDME dielectric constant (7.9) to predict the

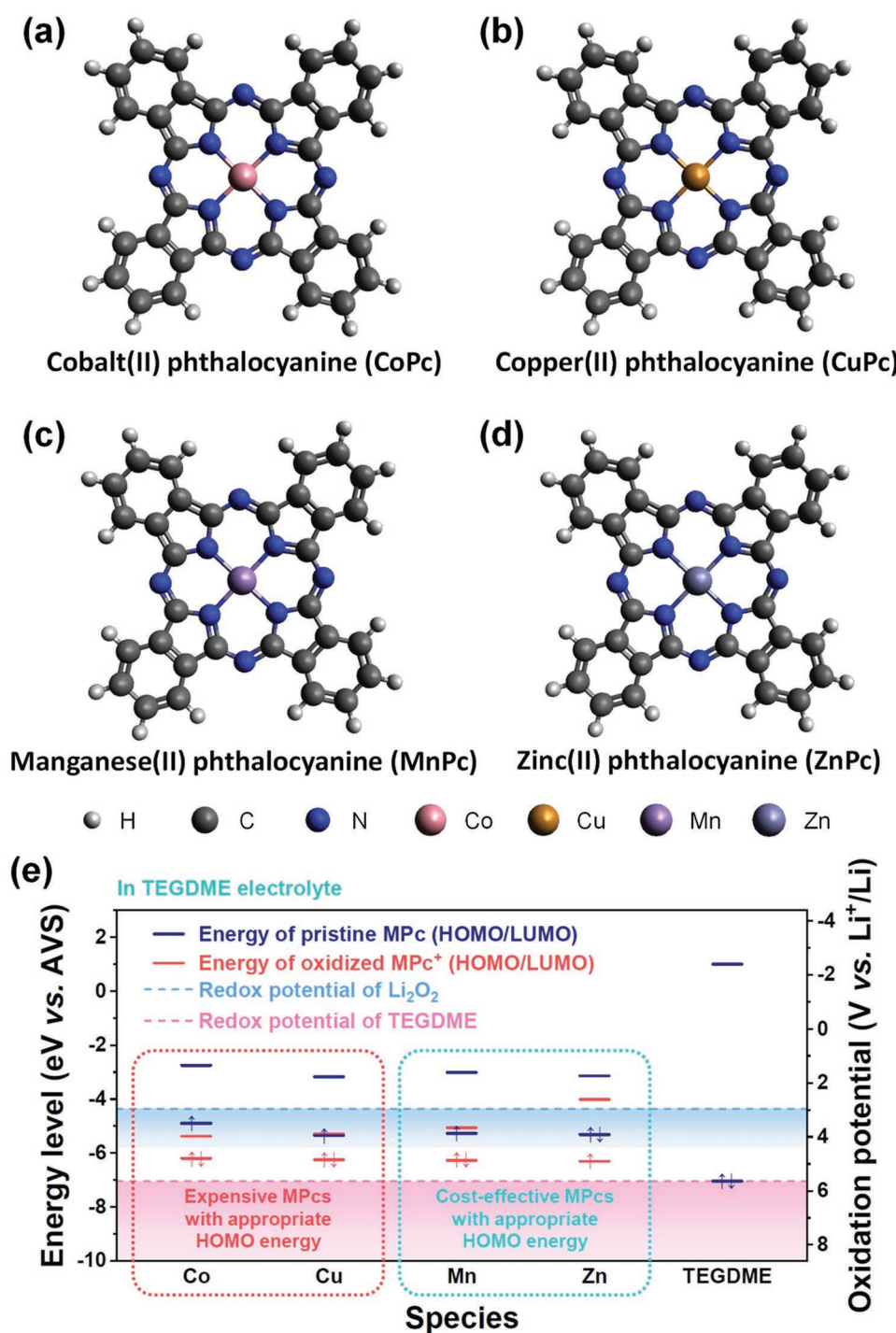


Figure 2. Molecular structures of a) CoPc, b) CuPc, c) MnPc, and d) ZnPc. e) DFT-based highest occupied molecular orbital (HOMO) and lowest unoccupied molecular orbital (LUMO) energies of pristine MPC and oxidized MPC⁺s in TEGDME.

theoretical energy levels of pristine MPCs and oxidized MPC⁺s. Reportedly, the catalytic activity of RM is determined by the relative energies between the pristine RM and oxidized RM⁺ in a specific electrolyte solvent.^[16]

Figure 2e presents the HOMO and lowest unoccupied molecular orbital (LUMO) energy levels of pristine MPCs (blue bar; vs absolute vacuum scale (AVS)) and oxidized MPC⁺s (red bar;

vs AVS). In addition, the numerical oxidation potentials (vs Li⁺/Li) corresponding to the HOMO and LUMO energy levels are listed in Table S1 (Supporting Information). To directly link the electrode potential for the electrochemical reaction to the chemical-reactivity-related HOMO/LUMO energy level, the AVS was set to ≈ -4.44 V compared to the standard hydrogen electrode (SHE).^[17] Notably, the cell operates at a given electrode potential

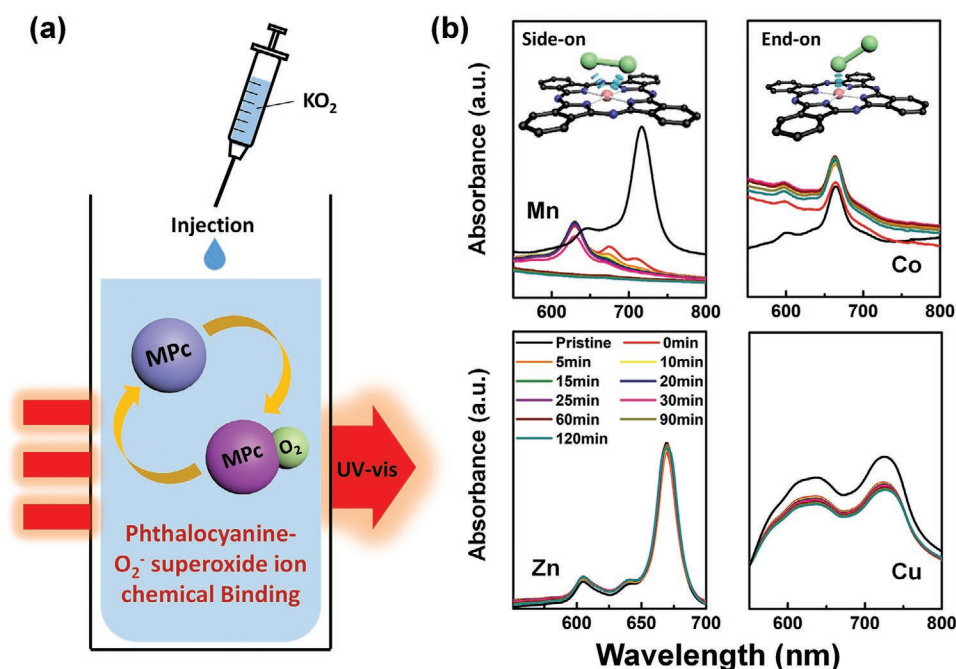


Figure 3. a) Schematic showing auto-oxygenated MPC properties after superoxide species was injected into electrolytes. b) UV-vis spectra of four MPCs at different times after superoxide injection. Wavelength range 550–800 nm was applied to all MPCs to detect the state of MPC central metal atoms. If states of central metals are altered, some peaks would shift or change in that range.

(U), and the free energy of the electrons in the electrode is governed by $\Delta G = -eU$. Therefore, the electron energy corresponding to the AVS is the opposite electrode potential. Based on this theory, the 0 V versus Li^+/Li is ≈ -1.39 eV versus AVS, and the Li_2O_2 formation redox potential ($1/2 \cdot \text{Li}_2\text{O}_2 \leftrightarrow \text{Li}^+ + e^- + 1/2 \cdot \text{O}_2$; 2.96 V vs Li^+/Li) could be set to ≈ -4.35 eV (versus AVS). According to Koopmans' theorem, the HOMO energy is equal to the ionization energy, which corresponds to the RM/RM $^+$ redox potential. Because the decomposition of Li_2O_2 occurs at ≈ 2.96 V (vs Li^+/Li ; dotted blue line) and the redox potentials of all the pristine MPCs are above ≈ 2.96 V, Li_2O_2 could decompose in the electrolyte consisting of TEGDME and MPCs. Furthermore, to prevent electrolyte oxidation and subsequent unwanted side reactions in Li– O_2 batteries, the HOMO energies of the oxidized MPC $^+$ s must be above that of the TEGDME (dotted red line; ≈ 5.71 V vs Li^+/Li).^[16] Otherwise, electrons are taken from TEGDME instead of the decomposition of Li_2O_2 , thereby severely decomposing the electrolyte. Because the HOMO energy levels of the oxidized MPC $^+$ s are above that of the TEGDME, they do not theoretically react with the electrolyte solvent, thereby enabling the stable operation of MPCs in LOB cells. Interestingly, among the Period 4 transition-metal-based MPCs, not only expensive Co- and Cu-based MPCs but also cost-effective Mn- and Zn-based MPCs delivered outstanding catalytic activities as promising RMs for application to LOBs. In addition, we used first-principles calculations to theoretically predict the variation in the charge densities of the oxidized MnPc and ZnPc (Figure S1, Supporting Information). In MnPc, the charge densities near the central Mn atom changed during oxidation because Mn is a transition metal, which can easily provide electrons. In ZnPc, on the other hand, the charge densities negligibly changed near the central Zn atom, which

exhibited a fixed valence state. Thus, these computational simulation results imply that the transition metals used in MPCs cannot only affect electron sharing during oxidation but also retain structural stability.

To confirm the computational simulation results, we performed real-time UV-vis spectrophotometry analysis on the MPCs and monitored the changes in absorbance at different times after oxygen binding. With the injection and subsequent dissociation of the KO_2 solution, the superoxide sources were supplied to the electrolyte (Figure 3a). The superoxide ions bound with MPC molecules through electron exchange, which structurally changed the MPCs, as determined by UV-vis absorbance (Figure 3b). Superoxide ions exhibit different binding properties depending on the d -orbital occupation of the central MPC metal atom.^[18] If the d -orbital is nonfilled and exhibits vacancies, the superoxide ions can attach to the transition-metal core by either “side-on” and “end-on.” For MnPc, the peak shifted between 550 and 800 nm after KO_2 was injected, which implies that the structure of the central Mn atom had changed by the reaction between the Mn ion and superoxide anions through the “side-on” configuration of the Mn ion and oxygen molecule (inset of Figure 3b).^[18–19] In a “side-on” configuration, because two oxygen ions bind the central metal atom at equal distances, the strong electronegativity of the oxygen ions can markedly affect the metal atom. Accordingly, the electronic structure of the MnPc is changed by the bound oxygen molecule, which shifts the corresponding peaks in the UV-vis spectra. In contrast, no peak shift was detected for CoPc and CuPc in the same range (550–800 nm), while the central metal ions had the open-shell d -orbitals. This result indicates that CoPc and CuPc are expected to bind through the “end-on” configuration, wherein one oxygen atom in an oxygen molecule

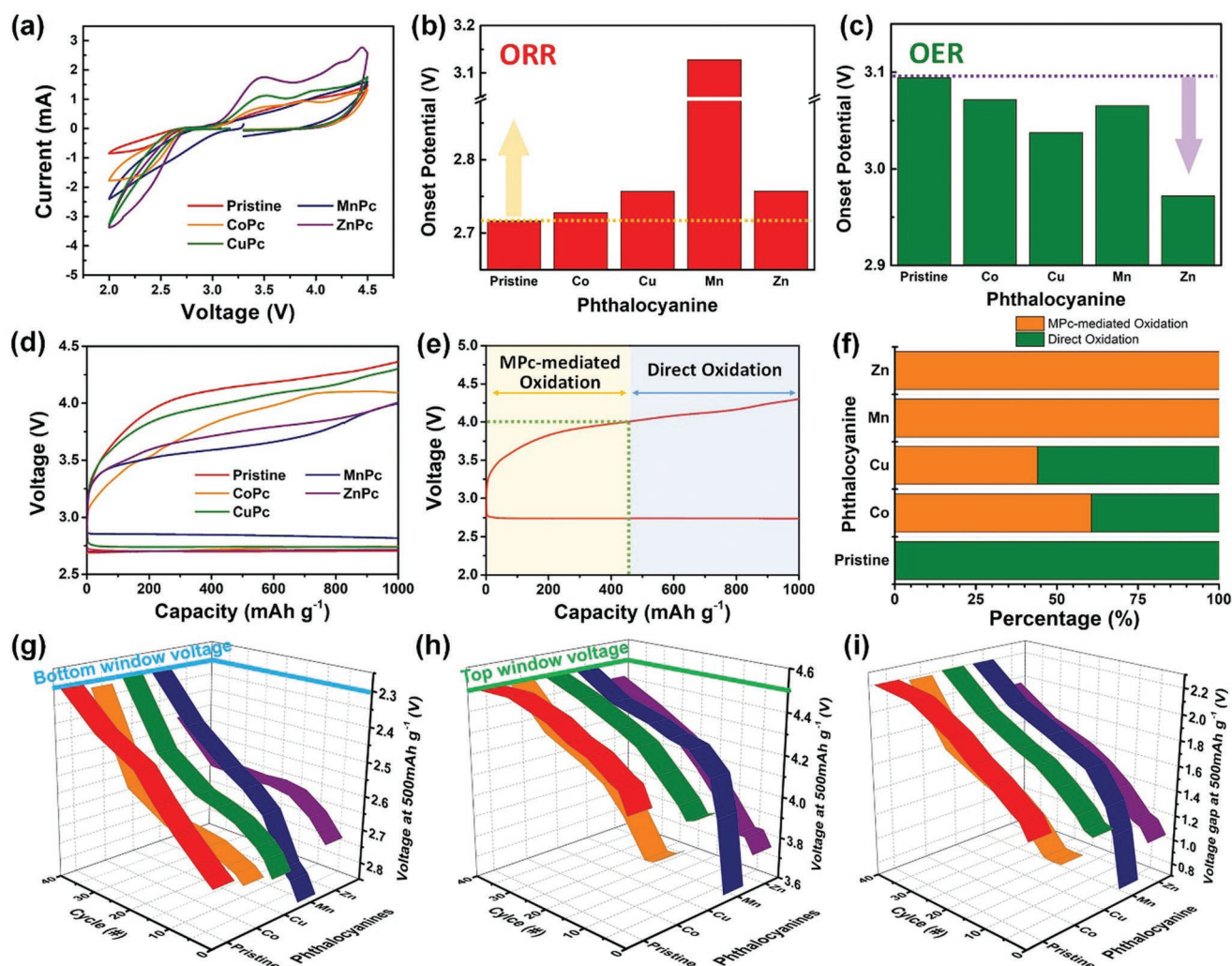


Figure 4. a) Cycle voltammetry (CV) curves obtained for Li–O₂ cells employing MPCs. CV-based comparison of onset potentials in b) ORR and c) OER regions of pristine and MPC-containing cells. d) Discharge–charge curves measured in window 2.3–4.5 V for Li–O₂ cells fabricated using pristine and MPC electrolytes. e, f) Ratios of “metal phthalocyanine-mediated oxidation (MPC-mediated oxidation)” and “direct oxidation” during charging of pristine and MPC-containing cells. Three-dimensional mapping cycling graphs collected during the middle of g) discharging and h) charging reactions for Li–O₂ batteries prepared with and without MPCs and i) corresponding voltage gap measured at 500 mA h⁻¹ during each cycle.

is bound to the MPC central transition-metal atom and the other oxygen atom is further away from the metal atom. This indicates the formation of the M–O–O (M: metal, O: oxygen) configuration (inset of Figure 3b), wherein the influence of the bound oxygen on the central metal atom is diminished, and the changes in the electronic structure of the core metal ions are negligible.^[19a,20] Thus, if the binding was related to the “end-on” configuration, the peak shift would be negligible in the UV–vis spectra despite the superoxide ion bound to the central metal ions. For ZnPc, the peak did not shift in the UV–vis spectra because the binding between the superoxide ion and the central Zn atom exhibiting fully filled *d*-orbitals could not be interpreted as a “side-on” or an “end-on” configuration.^[21] Instead, the side groups in the MPC molecular structures could participate in the electron transfer with superoxide ions through the following mechanisms: (i) a superoxide ion provides an electron to the ZnPc side chain, and the remaining O₂ is evolved, and (ii) a superoxide ion attaches itself to the ZnPc side group,

thereby changing the group electronic structure. Although binding slightly differs depending on the central metal ion, each central MPC metal ion clearly and uniquely reacts with superoxide ions, which indicates that MPCs could stabilize reactive oxygen radicals during the oxygen reduction reaction (ORR), and it can simultaneously suppress unwanted side reactions. Consequently, the MPCs stabilized the cell performance and achieved continuous cyclability.

2.2. Enhanced Electrochemical Properties of MPC-Containing LOBs

To confirm the redox properties and corresponding catalytic activities of the MPCs, we synthesized MPC-based electrolytes (Figure S2, Supporting Information) and performed cyclic voltammetry (CV) tests using LOB cells (Figure 4a; Figure S3, Supporting Information). The CV results indicate the typical

cathodic and anodic peaks of the reversible electrochemical reactions on the oxygen electrode surface ($2\text{Li}^+ + \text{O}_2 + 2\text{e}^- \leftrightarrow \text{Li}_2\text{O}_2$). In the cathodic region, the MPc-containing LOB cells exhibit drastically increased current density compared to the pristine LOB cells, implying that the MPcs enable more active ORRs in LOB cells. In the ORR, the onset potentials of the MPc-containing LOB cells were above those of the pristine ones (≈ 2.72 V). Notably, the MnPc-containing LOB cell exhibited the highest onset potential of ≈ 3.13 V (Figure 4b). Additional peaks are observed between 3.4 and 4.0 V in the anodic region, corresponding to MPc OER-based catalytic activities. All the MPc-containing LOB cells exhibited OER onset potentials below those of the pristine LOB cell (3.09 V). The ZnPc-containing LOB cell exhibited the lowest onset potential of ≈ 2.97 V (Figure 4c). The reduced gap between the ORR and OER onset potentials—corresponding to the decreased LOB-cell overpotential—was achieved using the MPcs as LOB RM catalysts. These results indicate that MPcs facilitate the formation and decomposition of lithium oxides (LiO_2 and Li_2O_2), thereby decreasing electrode polarization and improving electrochemical reversibility.

The charge–discharge curves are presented to further examine the electrochemical properties of the LOB cells fabricated using the MPc catalysts (Figure 4d). During discharging, all the discharge plateaus of the pristine and CoPc-, CuPc-, and ZnPc-containing LOB cells were similar to each other (≈ 2.72 V). For the MnPc-containing LOB cell, on the other hand, the discharge plateau is observed at ≈ 2.86 V, implying that MnPc is directly reduced instead of discharge products being formed. During discharging, the LOB cell fabricated using the MnPc soluble catalyst exhibits a higher redox potential than a typical pristine Li– O_2 cell, which can effectively reduce the cell overpotential. In addition, the MPcs decrease the LOB overpotential during charging. To distinguish the catalytic activity in the OER region rather than direct electrochemical decomposition of lithium oxide products, we arranged the ratio on two kinds of oxidation, named “MPc-mediated oxidation” and “direct oxidation” (Figure 4e; Figure S4, Supporting Information). MPc-mediated oxidation refers to oxidation facilitated by MPcs, and direct oxidation indicates Li_2O_2 oxidation in the pristine LOB-cell without catalyst components. Because the direct oxidation of Li_2O_2 usually occurs at above 4.0 V, we separated the two sorts of oxidations on the basis of 4.0 V and evaluated the dominant oxidation part during charge, comparing the corresponding “MPc-mediated oxidation” and “direct oxidation” (Figure 4f).^[22] Although the initial charge capacity is partially related to facile LiO_2 oxidation in the low-voltage range, the direct oxidation dominates pristine RM-free cells during charging. For MPc-containing LOB cells, on the other hand, because “MPc-mediated oxidation” and “direct oxidation” both considerably affect charging, we calculated and compared the capacity ratios of each “oxidation.” The CoPc- and CuPc-containing LOB cells exhibited ≈ 60.6 and $\approx 43.9\%$ MPc-mediated oxidation during early charging, respectively. The oxidized MPc⁺ species chemically withdrew electrons from the lithium oxide products and subsequently decomposed them into Li^+ and O_2 . For the latter 50% of the charge region, Li_2O_2 products were directly oxidized, and two different plateaus appeared in the charge profile, which indicates CoPc- or CuPc-assisted

reactions and direct Li_2O_2 oxidation, respectively (Figure S4, Supporting Information). During the direct oxidation of Li_2O_2 , the O_2^- intermediate can coordinate with MPcs and then O_2 gas is evolved by the reverse oxidation of the reduced MPcs.^[23] For MnPc and ZnPc, the charge processes are fully mediated by the MPc (i.e., 100% MPc-mediated oxidation), thereby maintaining charging potentials below 4.0 V until charging is terminated by controlling the capacity limit. The consistent MnPc- and ZnPc-mediated charging during the overall anodic reaction enables the superior catalytic activities of the oxidation-mediating RMs for application to LOBs.

To elucidate the reversibility of the MPc-containing LOBs, we compared the changes in the voltage of the MPc-containing LOBs as a function of the number of cycles (Figures 4g–i; Figures S5 and S6, Supporting Information). Figure 4g,h represents the voltages of different MPc-RMs collected in the middle of the discharge and charge reaction (at 500 mAh g^{-1}) of each cycle, respectively. During discharging, a good RM should enable high LOB discharge potentials and exhibit a gradually decreasing voltage graph. Although the MnPc-containing LOBs exhibited outstanding performance during early cycling [voltages ≈ 2.8 and ≈ 3.6 V during discharging and charging, respectively, at the halfway point (500 mAh g^{-1})], the voltage gradually degraded and the overpotential increased after several cycles, which implies that the MnPc structure was relatively unstable during repeated LOB charge–discharge cycling. Interestingly, the ZnPc-containing LOBs still retained ORR and OER operation voltages after the 40th cycle compared to the other MPcs. Moreover, we compared the overpotential degrees of the MPc-containing LOB cells by summarizing the previous two graphs (Figure 4i). The MPc-containing LOB cells exhibited better cyclability with stable energy efficiency and a lower voltage gap between the discharge and subsequent charge than the pristine LOB cells, which indicates the outstanding LOB MPc catalytic activity (Figure S6, Supporting Information). Furthermore, the ZnPc-containing LOBs exhibited a moderately reduced overpotential and outstanding stability, while the MnPc provided superior catalytic performance and insufficient durability for application to LOBs.

According to the electrochemical results shown in Figure 4, we supposed that the LAB electrochemical performance could be further enhanced by blending MnPc and ZnPc, compared to using only MPc (Figure 5a). To confirm the synergetic and collaborative effects of the blended MnPc/ZnPc, we performed CV tests under a low- O_2 (<20 vol.%) purging condition like ambient air. Figure 5b shows that blending the MnPc and ZnPc results in an OER onset potential of only ≈ 3.28 V, which is the lowest among all the LAB cells. The ORR onset potential of the blended MnPc/ZnPc-containing cell is ≈ 3.1 V, which is the highest among all the LAB cells. Interestingly, the blended MnPc/ZnPc-containing LAB cell exhibited a much smaller gap of ≈ 0.18 V between the OER and ORR onset potentials than the pristine (≈ 0.85 V), MnPc-containing (≈ 0.24 V), and ZnPc-containing (≈ 0.75 V) LAB cells, indicating that the MnPc/ZnPc-containing LAB cell exhibited enhanced reversibility during both discharging and charging. To further investigate the impact of the blended MnPc/ZnPc on the electrochemical performance, we performed charge–discharge tests in ambient air at a limited capacity of 1000 mAh g^{-1} (Figure 5c). Although

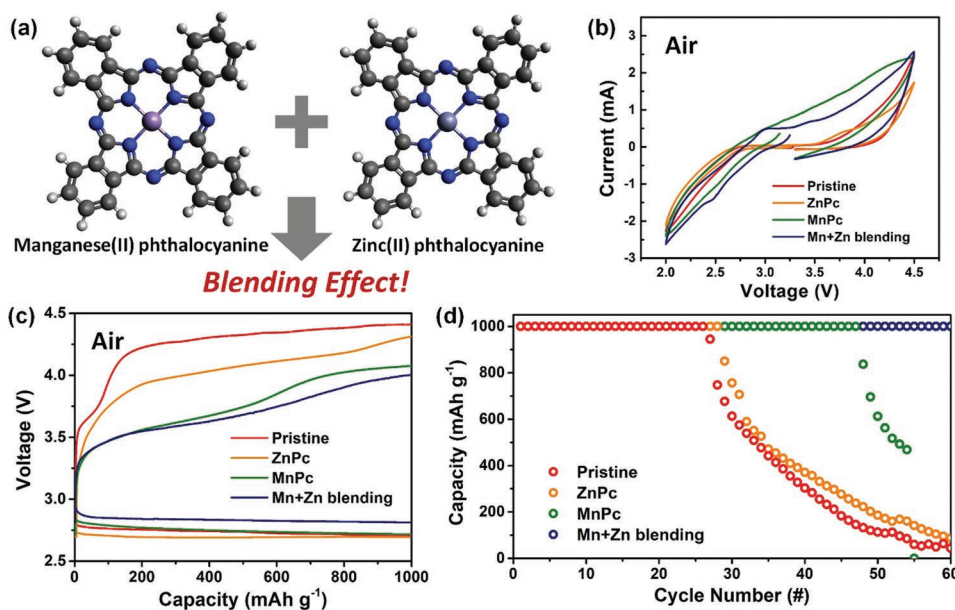


Figure 5. a) Mixing MnPc and ZnPc to synergistically improve cell reactions. b) CV curves, c) discharging–charging curves, and d) cycling performances of Li air-breathing cells fabricated using pristine, ZnPc, MnPc, and ZnPc + MnPc blended electrolytes.

the MnPc and ZnPc individually offered outstanding catalytic activities in the OER region (even in a low-O₂ atmosphere), the blended MnPc/ZnPc catalyst enabled far superior catalytic activation for the ORR and OER and exceptionally decreased overpotentials. Moreover, the application of the blended MnPc/ZnPc enhanced the cycling performance of LABs. As shown in Figure 5d, the capacity of the blended MnPc/ZnPc-containing LAB was stably retained for more than 60 cycles with a limited capacity of 1000 mAh g⁻¹, whereas the capacities of the pristine and ZnPc-containing LABs were severely degraded before 30 cycles. Moreover, the MnPc-containing LAB exhibited drastic capacity degradation after 50 cycles. These outstanding results of MnPc/ZnPc-containing LAB cell exceed the performance of conventional RMs in Li–air reactions and suggest that suitably blending different MPc catalysts can maximize the performance of air-breathing batteries, thereby offering a hint for optimizing RM catalysts.

2.3. Reaction Mechanism of MPc-Containing LABs

To examine the changes in the electrode chemical bonding in different electrochemical states, we performed ex situ X-ray photoelectron spectroscopy (XPS; Figures S7a–c, Supporting Information). In the C 1s spectra, the pristine, discharged, and charged electrodes all showed common peaks corresponding to C–C and C–O bonds. The intensity of the C–C peak decreased during discharging because the discharge products covered the carbon electrode surface. A weak peak corresponding to the lithium carbonate (Li₂CO₃) side product was also detected during discharging. Likewise, the peak representing the PVdF binder also weakened after discharging because the electrode surface was covered by the discharge products. After charging, the C–C peak intensity was increased and the Li₂CO₃ peak completely

disappeared, thereby implying the reversible decomposition of the discharge products in the blended MnPc/ZnPc-containing LAB cell. Similarly, in the Li 1s spectra, peaks related to discharge products such as lithium peroxide (Li₂O₂) and lithium carbonate (Li₂CO₃) were observed after discharging and completely disappeared during charging. The reversible formation and decomposition of the discharge products were also well matched with the peaks in the O 1s spectra. As shown in Figure S7c (Supporting Information), peaks attributed to discharge products (Li₂CO₃ and Li₂O₂) appeared after discharging and completely disappeared after charging. To observe the morphological changes of the electrode surfaces, we performed ex situ scanning electron microscopy (SEM) on the pristine, discharged, and charged electrodes (Figures S7d–f, Supporting Information). During discharging, the Ni foam substrate was covered with the discharge products, and the original surface was reversibly recovered after charging, thereby suggesting that the blended MnPc/ZnPc could be applied as a promising and effective RM to LABs to highly enhance LAB electrochemical performances—even under harsh conditions exhibiting <20 vol.% O₂.

To further validate the LAB MPc reaction mechanisms, we calculated the Gibbs free energies of each intermediate and presented the changes in the Gibbs free energies in Figure 6 and Figure S8 (Supporting Information). For the MnPc- and ZnPc-mediated ORRs, the entire energy-level profile decreases, indicating that the LABs spontaneously react with the MPc–RMs (Figure 6a,b). The highly reactive oxygen radicals are stabilized by MPc–O₂ binding and subsequently react with nearby Li ions to form lithium oxide products (mainly LiO₂ and Li₂O₂). The remarkably decreased adsorption energies (–2.14355 and –1.75697 eV for MnPc and ZnPc, respectively) support the outstanding oxygen-binding properties and resulting synergies of the blended MnPc/ZnPc catalyst in LABs operating in a low-oxygen atmosphere (Figure 6c).

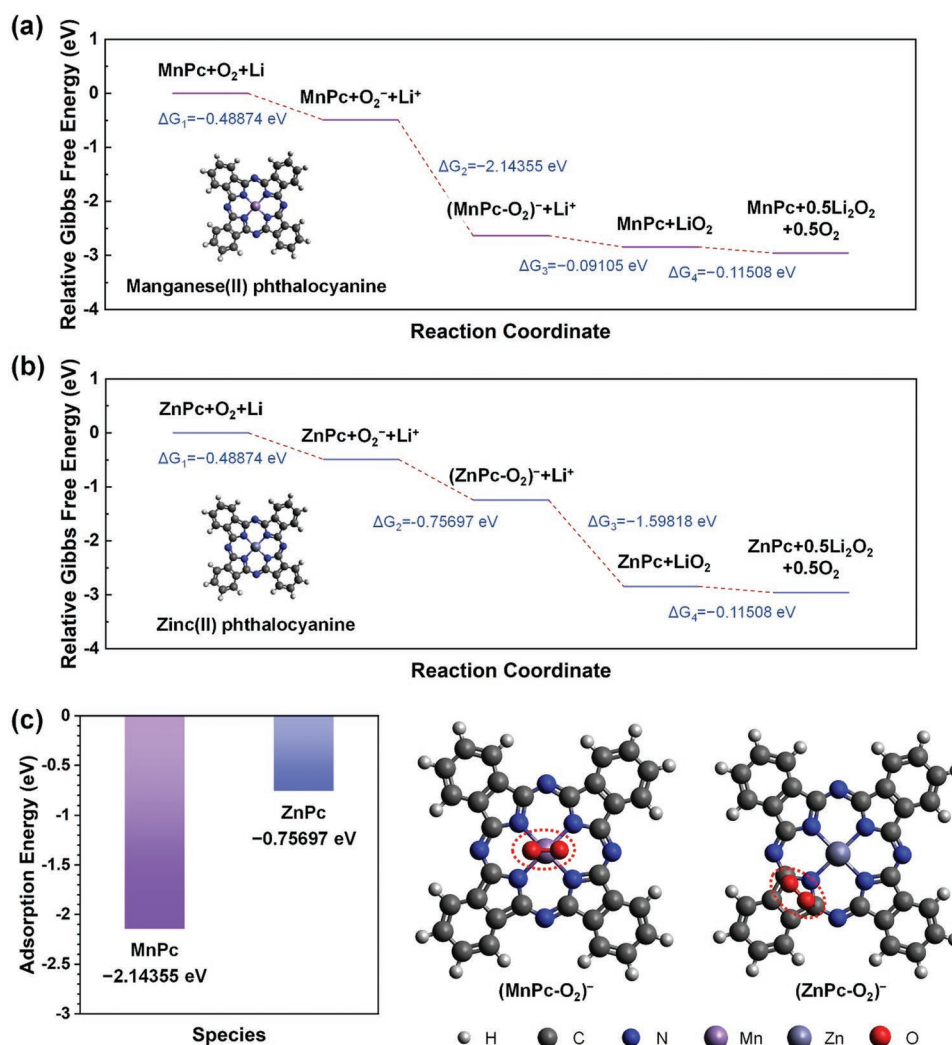


Figure 6. Relative Gibbs free-energy diagrams generated for cell-reaction intermediates in a) MnPc- and b) ZnPc-containing Li-O₂ batteries. c) Decreased adsorption energies of MnPc and ZnPc after binding with oxygen radicals and molecular structures of (MnPc-O₂)⁻ and (ZnPc-O₂)⁻ bound states.

Interestingly, the oxygen-binding site of MnPc is the central metal ion. In contrast, the ZnPc molecule attaches to the surrounding porphyrin rings. In the opposite OER, the discharge products lose electrons and decompose into Li-ions and oxygen, thereby returning to a higher energy level during charging. Other MPc-containing cells (CoPc and CuPc) also spontaneously reacted facilitated by the catalytic reactions between the MPc and the oxygen in the LABs (Figure S8, Supporting Information). The entire reaction mechanism of the MPc-containing LABs is summarized in Figure S9 (Supporting Information). During the ORR, MPcs bind to and stabilize oxygen radicals to prevent unwanted side reactions. The subsequent OER proceeds following two mechanisms. In the MPc-mediated OER, MPc is oxidized to MPc⁺ and chemically reacts with discharge products (usually Li₂O₂), thereby acting as a conventional RM. However, in direct oxidation in MPc-containing cells, the discharge products are preferentially decomposed into Li-ions and oxygen radicals, just like in an RM-free OER. Then, the MPcs chemically associate with oxygen radicals, thereby binding with oxygen to form MPc-O₂

and stabilizing the reactive intermediates—like in the ORR. Owing to their unique functionality, MPc molecules effectively catalyze both reaction pathways during charging, which enables both electrochemical redox reactions and auto-binding with superoxide intermediates.

3. Conclusion

In summary, we optimized the catalytic activity of metal phthalocyanine complexes as RMs—electrolyte catalysts for Li air-breathing batteries—and tuned the central atom using Period 4 transition-metal components (Co, Cu, Mn, and Zn). By analyzing the structures and molecular orbital (HOMO and LUMO) levels of each MPc in the TEGDME electrolyte, we verified that the MPc complexes were suitable for promoting stable and enhanced Li-O₂ cell reactions. We also used UV-vis spectrometry to investigate in real-time the chemically active oxygen binding of each MPc after injecting superoxide species into the electrolyte. The superoxide species bound

to the central metal atom in the MPCs, which exhibited different binding properties and sites depending on the *d*-orbital occupation of the metal atom. In agreement with theoretical predictions, the Li–O₂ cells fabricated using MPCs exhibited reduced overpotentials during charging owing to MPC-mediated oxidation, and the MPC catalytic activities varied depending on the central metal atom. The catalytic activity was maximized by blending MnPc and ZnPc and showed markedly high catalytic activities in both the ORR and OER regions. Consequently, the blended catalyst achieved excellent cell performance even in low-O₂ (<20 vol.%) ambient air. The reversible formation and decomposition of discharge products were confirmed by the ex situ characterization of cells fabricated using the blended MPCs. A detailed reaction mechanism was also suggested based on the calculated energy diagram and various experimental measurements. This study provides key knowledge for understanding organometallic porphyrin-based materials as eco-friendly and nature-derived catalysts, and verifies their potential as a suitable alternative catalyst to fabricate efficient Li–O₂/air-breathing batteries exhibiting exceptional energy storage.

4. Experimental Section

Materials and Chemicals: Co, Cu, Mn, and Zn phthalocyanines, tetraethylene glycol dimethyl ether (TEGDME, 99%), bis(trifluoromethane) sulfonimide lithium salt (LiTFSI, 99.95%), poly(vinylidene fluoride) (PVdF, $M_w \approx 180000$), *N*-methyl-2-pyrrolidone (NMP, anhydrous, 99.5%), and potassium dioxide (KO₂) were purchased from Sigma–Aldrich (Korea). Residual moisture was removed from the TEGDME by dipping freshly activated molecular sieves (4 Å) into the solvent for 2 weeks.

Preparation of Li–O₂/Li–Air Cells: The oxygen/air electrode was fabricated using multiwalled carbon nanotubes (MWCNTs, 90 wt.%) and PVdF (10 wt.%) dissolved in NMP. The slurry was pasted onto a Ø12-mm Ni-foam current collector and was dried overnight at 80 °C under vacuum condition. The average slurry mass loading was 0.4 mg per Ø12-mm Ni foam. The pristine electrolyte was fabricated using LiTFSI dissolved in TEGDME (1 M) and stirred for 24 h at room temperature. For the MPC-containing electrolyte, phthalocyanine (0.1 g) and LiTFSI (1 M) were diluted in TEGDME (0.5 mL) and were stirred for 24 h in an Ar-filled glovebox to saturate the precursor solution. For the MPC-blended electrolyte, equal volumes of MnPc and ZnPc electrolytes (0.5 mL) were uniformly mixed. The supernatant of the saturated MPC electrolyte was used in both the single and blended MPC electrolytes. A Ø12-mm Li-metal foil was used as the anode, and a glass fiber (Whatman GF/A microfiber filter paper) was used as the separator. Coin cells containing several holes were used for cyclic voltammetry (CV), full discharging–charging, and cycling tests. All the cells were assembled in an Ar-filled glovebox. The cells were purged with O₂ (99.999%) and air (21% O₂, 79% N₂) before testing.

Materials Characterization: XPS (K-alpha, Thermo U.K.) was performed to characterize and analyze the electrode surfaces. The MWCNT-loaded electrodes were observed using field-emission SEM (FE-SEM). To investigate the oxygen-binding effect of the phthalocyanine, UV–vis spectrophotometer (UV-2550, Shimadzu) was used.

Electrochemical Characterization: The catalytic activity of the MPC-containing LAB cells was analyzed using cyclic voltammetry (Biologic VSP potentiostat with an impedance function) in the range 2.0–4.5 V and at increasing scan rates up to 100 mV s^{−1}. The charging–discharging tests were performed using a potentiostat/galvanostat (WonATech, Co., Ltd., WBCS3000, Korea) at 100 mA g^{−1} in the range 2.3–4.5 V versus Li/Li⁺. For the cycling tests, a potentiostat/galvanostat (WonATech, Co., Ltd., WBCS3000L, Korea) was used at 100 mA g^{−1} with a limited capacity

of 1000 mAh g^{−1} in the same voltage range as the charging–discharging tests. Before the electrochemical tests, the cells were purged with O₂ gas/air, and the tests were performed at room temperature.

Computational Details: For the RM molecules, the geometry was optimized and the energy was evaluated using the Gaussian 16 software package.^[24] For all the calculations, spin-unrestricted density functional theory (DFT) was performed based on the Becke–Lee–Yang–Parr (B3LYP) hybrid exchange–correlation functional^[25] and the triple-zeta valence polarization (TZVP) basis set.^[26] The molecular structures of the calculated MPC–RMs were visualized using Avogadro software.^[27] The TEGDME solvation was considered by applying a dielectric constant of 7.9, as used in previous studies.^[16,28]

Ex Situ Characterization: The surfaces characterization of the cycled electrodes were characterized using XPS. The cycled surface morphologies were observed using SEM. The samples were cycled by galvanostatic discharging and charging at 100 mA g^{−1}, and each electrode was collected after the initial discharging and charging cycles conducted with no capacity limit. A pristine electrode was dipped into the electrolyte to prepare a control sample. Like the pristine electrode, the discharged and charged cells were disassembled in an Ar-filled glovebox.

Time-Course UV–vis Spectroscopy: The concentration of phthalocyanines was diluted in TEGDME (0.38×10^{-4} M) and LiTFSI/TEGDME (1 M) to generate UV–vis spectra. Overall, KO₂ (5×10^{-3} M) was dissolved in TEGDME for 24 h in an Ar-filled glovebox to saturate the precursor solution. Electrolyte solutions (2.5 mL) were added to quartz cuvettes, which were tightly sealed with septum caps. A syringe was used to inject the KO₂ supernatant (0.5 mL) into the cuvettes, and the UV–vis spectra were measured for 2 h.

Supporting Information

Supporting Information is available from the Wiley Online Library or from the author.

Acknowledgements

H.-S.K. and B.K. contributed equally to this work. This work was supported by the National Research Foundation of Korea (NRF) grant funded by the Korean government (MSIT) (No. 2019R1C1C1007886, 2019M3D1A2104105, and 2018R1A5A1025224). The calculation resources were supported by the Supercomputing Center in Korea Institute of Science and Technology Information (KSC-2021-CRE-0171).

Conflict of Interest

The authors declare no conflict of interest.

Data Availability Statement

The data that support the findings of this study are available from the corresponding author upon reasonable request.

Keywords

air-breathing batteries, lithium–oxygen batteries, metal phthalocyanine, oxygen-binding catalysts, porphyrin

Received: November 10, 2021
Revised: December 9, 2021
Published online: January 5, 2022

- [1] a) J.-M. Tarascon, M. Grätzel, *Materials for sustainable energy: a collection of peer-reviewed research and review articles from Nature Publishing Group, World Scientific*, Macmillan Publishers, Ltd, London, UK **2011**; b) M. M. Thackeray, C. Wolverton, E. D. Isaacs, *Energy Environ. Sci.* **2012**, 5, 7854; c) X. Shen, H. Liu, X.-B. Cheng, C. Yan, J.-Q. Huang, *Energy Stor. Mater.* **2018**, 12, 161; d) R. Chen, T. Zhao, F. Wu, *Chem. Commun.* **2015**, 51, 18; e) H.-S. Kim, J.-Y. Lee, J.-K. Yoo, W.-H. Ryu, *ACS Mater. Lett.* **2021**, 3, 815; f) J.-Y. Lee, H.-S. Kim, J.-S. Lee, C.-J. Park, W.-H. Ryu, *ACS Sustainable Chem. Eng.* **2019**, 7, 16151.
- [2] a) D. U. Lee, P. Xu, Z. P. Cano, A. G. Kashkooli, M. G. Park, Z. Chen, *J. Mater. Chem. A* **2016**, 4, 7107; b) J. Lu, Y. J. Lee, X. Luo, K. C. Lau, M. Asadi, H.-H. Wang, S. Brombosch, J. Wen, D. Zhai, Z. Chen, *Nature* **2016**, 529, 377; c) W.-J. Kwak, Rosy, D. S. , C. Xia, H. Kim, L. R. Johnson, P. G. Bruce, L. F. Nazar, Y.-K. Sun, A. A. Frimer, *Chem. Rev.* **2020**, 120, 6626; d) S. Ding, X. Yu, Z.-F. Ma, X. Yuan, *J. Mater. Chem. A* **2021**, 9, 8160; e) P. G. Bruce, S. A. Freunberger, L. J. Hardwick, J.-M. Tarascon, *Nat. Mater.* **2012**, 11, 19.
- [3] a) W.-H. Ryu, T.-H. Yoon, S. H. Song, S. Jeon, Y.-J. Park, I.-D. Kim, *ACS Nano Lett.* **2013**, 13, 4190; b) T. Zhang, H. Zhou, *Angew. Chem., Int. Ed.* **2012**, 51, 11062.
- [4] a) R. Padbury, X. Zhang, *J. Power Sources* **2011**, 196, 4436; b) G. Girishkumar, B. McCloskey, A. C. Luntz, S. Swanson, W. Wilcke, *J. Phys. Chem. Lett.* **2010**, 1, 2193.
- [5] a) J.-S. Lee, H.-S. Kim, W.-H. Ryu, *Appl. Surf. Sci.* **2019**, 466, 562; b) J.-S. Lee, C. Lee, J.-Y. Lee, J. Ryu, W.-H. Ryu, *ACS Catal.* **2018**, 8, 7213; c) R. Black, J. H. Lee, B. Adams, C. A. Mims, L. F. Nazar, *Angew. Chem., Int. Ed.* **2013**, 52, 392; d) H. D. Lim, H. Song, J. Kim, H. Gwon, Y. Bae, K. Y. Park, J. Hong, H. Kim, T. Kim, Y. H. Kim, *Angew. Chem.* **2014**, 126, 4007; e) L.-N. Song, W. Zhang, Y. Wang, X. Ge, L.-C. Zou, H.-F. Wang, X.-X. Wang, Q.-C. Liu, F. Li, J.-J. Xu, *Nat. Commun.* **2020**, 11, 2191; f) J. Mei, J. Wang, H. Gu, Y. Du, H. Wang, Y. Yamauchi, T. Liao, Z. Sun, Z. Yin, *Adv. Mater.* **2021**, 33, 2004920; g) J. Mei, T. Liao, J. Liang, Y. Qiao, S. X. Dou, Z. Sun, *Adv. Energy Mater.* **2020**, 10, 1901997.
- [6] a) H.-G. Jung, Y. S. Jeong, J.-B. Park, Y.-K. Sun, B. Scrosati, Y. J. Lee, *ACS Nano* **2013**, 7, 3532; b) Y.-C. Lu, H. A. Gasteiger, Y. Shao-Horn, *J. Am. Chem. Soc.* **2011**, 133, 19048; c) Y.-C. Lu, B. M. Gallant, D. G. Kwabi, J. R. Harding, R. R. Mitchell, M. S. Whittingham, Y. Shao-Horn, *Energy Environ. Sci.* **2013**, 6, 750; d) Z. Shi, W. Yang, Y. Gu, T. Liao, Z. Sun, *Adv. Sci.* **2020**, 7, 2001069.
- [7] a) F. Mizuno, S. Nakanishi, Y. Kotani, S. Yokoishi, H. Iba, *Electrochemistry* **2010**, 78, 403; b) S. A. Freunberger, Y. Chen, N. E. Drewett, L. J. Hardwick, F. Bardé, P. G. Bruce, *Angew. Chem., Int. Ed.* **2011**, 50, 8609; c) S. A. Freunberger, Y. Chen, Z. Peng, J. M. Griffin, L. J. Hardwick, F. Bardé, P. Novák, P. G. Bruce, *J. Am. Chem. Soc.* **2011**, 133, 8040; d) J. Xiao, J. Hu, D. Wang, D. Hu, W. Xu, G. L. Graff, Z. Nie, J. Liu, J.-G. Zhang, *J. Power Sources* **2011**, 196, 5674.
- [8] a) J. B. Park, S. H. Lee, H. G. Jung, D. Aurbach, Y. K. Sun, *Adv. Mater.* **2018**, 30, 1704162; b) W.-J. Kwak, H. Kim, H.-G. Jung, D. Aurbach, Y.-K. Sun, *J. Electrochem. Soc.* **2018**, 165, A2274; c) M. J. Trahan, S. Mukerjee, E. J. Plichta, M. A. Hendrickson, K. Abraham, *J. Electrochem. Soc.* **2012**, 160, A259; d) B. D. McCloskey, R. Scheffler, A. Speidel, D. S. Bethune, R. M. Shelby, A. C. Luntz, *J. Am. Chem. Soc.* **2011**, 133, 18038.
- [9] a) Y. Ko, H. Park, B. Kim, J. S. Kim, K. Kang, *Trends Chem* **2019**, 1, 349; b) I. Landa-Medrano, I. Lozano, N. Ortiz-Vitoriano, I. R. de Larramendi, T. Rojo, *J. Mater. Chem. A* **2019**, 7, 8746; c) J.-H. Kang, J. Lee, J.-W. Jung, J. Park, T. Jang, H.-S. Kim, J.-S. Nam, H. Lim, K. R. Yoon, W.-H. Ryu, *ACS Nano* **2020**, 14, 14549.
- [10] X. Gao, Y. Chen, L. R. Johnson, Z. P. Jovanov, P. G. Bruce, *Nat. Energy* **2017**, 2, 17118.
- [11] a) W.-J. Kwak, H. Kim, Y. K. Petit, C. Leypold, T. T. Nguyen, N. Mahne, P. Redfern, L. A. Curtiss, H.-G. Jung, S. M. Borisov, *Nat. Commun.* **2019**, 10, 1380; b) N. Feng, P. He, H. Zhou, *ChemSusChem* **2015**, 8, 600; c) D. Kundu, R. Black, B. Adams, L. F. Nazar, *ACS Cent. Sci.* **2015**, 1, 510; d) W.-J. Kwak, S. A. Freunberger, H. Kim, J. Park, T. T. Nguyen, H.-G. Jung, H. R. Byon, Y.-K. Sun, *ACS Catal.* **2019**, 9, 9914.
- [12] a) D. Sun, Y. Shen, W. Zhang, L. Yu, Z. Yi, W. Yin, D. Wang, Y. Huang, J. Wang, D. Wang, *J. Am. Chem. Soc.* **2014**, 136, 8941; b) S. Matsuda, S. Mori, Y. Kubo, K. Uosaki, K. Hashimoto, S. Nakanishi, *Chem. Phys. Lett.* **2015**, 620, 78; c) S. Matsuda, S. Mori, K. Hashimoto, S. Nakanishi, *J. Phys. Chem. C* **2014**, 118, 28435; d) K. P. Yao, J. T. Frith, S. Y. Sayed, F. Bardé, J. R. Owen, Y. Shao-Horn, N. Garcia-Araez, *J. Phys. Chem. C* **2016**, 120, 16290; e) W.-J. Kwak, A. Mahammed, H. Kim, T. T. Nguyen, Z. Gross, D. Aurbach, Y.-K. Sun, *Mater. Horiz.* **2020**, 7, 214.
- [13] a) J. L. Sessler, D. Seidel, *Angew. Chem., Int. Ed.* **2003**, 42, 5134; b) A. B. Sorokin, *Chem. Rev.* **2013**, 113, 8152.
- [14] Z. Zhang, L. Kong, Y. Xiong, Y. Luo, J. Li, *Solid State Electrochem.* **2014**, 18, 3471.
- [15] a) D. A. Kuznetsov, B. Han, Y. Yu, R. R. Rao, J. Hwang, Y. Román-Leshkov, Y. Shao-Horn, *Joule* **2018**, 2, 225; b) Z. Xu, G. Zhang, Z. Cao, J. Zhao, H. Li, *J. Mol. Catal. A: Chem.* **2010**, 318, 101; c) M. Nabid, R. Sedghi, P. Jamaat, N. Safari, A. Entezami, *Appl. Catal. A: Gen* **2007**, 328, 52.
- [16] H.-D. Lim, B. Lee, Y. Zheng, J. Hong, J. Kim, H. Gwon, Y. Ko, M. Lee, K. Cho, K. Kang, *Nat. Energy* **2016**, 1, 16066.
- [17] a) S. Trasatti, *Pure Appl. Chem.* **1986**, 58, 955; b) A. Khetan, H. Pitsch, V. Viswanathan, *J. Phys. Chem. Lett.* **2014**, 5, 1318.
- [18] P. S. Miedema, M. M. van Schooneveld, R. Bogerd, T. C. Rocha, M. Hävecker, A. Knop-Gericke, F. M. de Groot, *J. Phys. Chem. C* **2011**, 115, 25422.
- [19] a) J. P. Collman, R. R. Gagne, C. A. Reed, W. T. Robinson, G. A. Rodley, *Proc. Natl. Acad. Sci. U.S.A.* **1974**, 71, 1326; b) J. Griffith, *Proc. R. Soc. Lond. A Math. Phys. Sci.* **1956**, 235, 23.
- [20] J. J. Weiss, *Nature* **1964**, 202, 83.
- [21] S. Yu, S. Ahmadi, C. Sun, P. T. Z. Adibi, W. Chow, A. Pietzsch, M. Göthelid, *J. Chem. Phys.* **2012**, 136, 154703.
- [22] a) Y. Wang, N.-C. Lai, Y.-R. Lu, Y. Zhou, C.-L. Dong, Y.-C. Lu, *Joule* **2018**, 2, 2364; b) C. Laoire, S. Mukerjee, E. J. Plichta, M. A. Hendrickson, K. Abraham, *J. Electrochem. Soc.* **2011**, 158, A302; c) K. Abraham, Z. Jiang, *J. Electrochem. Soc.* **1996**, 143, 1.
- [23] W.-H. Ryu, F. S. Gittleson, J. M. Thomsen, J. Li, M. J. Schwab, G. W. Brudvig, A. D. Taylor, *Nat. Commun.* **2016**, 7, 12925.
- [24] M. J. Frisch, G. W. Trucks, H. B. Schlegel, G. E. Scuseria, M. A. Robb, J. R. Cheeseman, G. Scalmani, V. Barone, G. A. Petersson, H. Nakatsuji, X. Li, M. Caricato, A. V. Marenich, J. Bloino, B. G. Janesko, R. Gomperts, B. Mennucci, H. P. Hratchian, J. V. Ortiz, A. F. Izmaylov, J. L. Sonnenberg, D. Williams-Young, F. Ding, F. Lipparini, F. Egidi, J. Goings, B. Peng, A. Petrone, T. Henderson, D. Ranasinghe, V. G. Zakrzewski, J. Gao, N. Rega, G. Zheng, W. Liang, M. Hada, M. Ehara, K. Toyota, R. Fukuda, J. Hasegawa, M. Ishida, T. Nakajima, Y. Honda, O. Kitao, H. Nakai, T. Vreven, K. Throssell, J. A. Montgomery Jr., J. E. Peralta, F. Ogliaro, M. J. Bearpark, J. J. Heyd, E. N. Brothers, K. N. Kudin, V. N. Staroverov, T. A. Keith, R. Kobayashi, J. Normand, K. Raghavachari, A. P. Rendell, J. C. Burant, S. S. Iyengar, J. Tomasi, M. Cossi, J. M. Millam, M. Klene, C. Adamo, R. Cammi, J. W. Ochterski, R. L. Martin, K. Morokuma, O. Farkas, J. B. Foresman, D. J. Fox, Gaussian, Inc., Wallingford CT, U.S.A., *Gaussian 16, Revision C.01*, **2016**.
- [25] a) P. J. Stephens, F. J. Devlin, C. F. Chabalowski, M. J. Frisch, *J. Phys. Chem. A* **1994**, 98, 11623; b) C. Lee, W. Yang, R. G. Parr, *Phys. Rev. B* **1988**, 37, 785; c) A. D. Beck, *J. Chem. Phys.* **1993**, 98, 5648.
- [26] a) A. Schäfer, C. Huber, R. Ahlrichs, *J. Chem. Phys.* **1994**, 100, 5829; b) A. Schäfer, H. Horn, R. Ahlrichs, *J. Chem. Phys.* **1992**, 97, 2571; c) B. Klauwünzer, D. Kröner, P. Saalfrank, *J. Phys. Chem. B* **2010**, 114, 10826.
- [27] M. D. Hanwell, D. E. Curtis, D. C. Lonie, T. Vandermeersch, E. Zurek, G. R. Hutchison, *J. Cheminformatics* **2012**, 4, 17.
- [28] M. Lee, J. Hong, B. Lee, K. Ku, S. Lee, C. B. Park, K. Kang, *Green Chem.* **2017**, 19, 2980.